

Seismic signatures of two orthogonal sets of vertical microcorrugated fractures

Rodrigo Felício Fuck and Ilya Tsvankin

Center for Wave Phenomena, Department of Geophysics, Colorado School of Mines, Golden, CO 80401

ABSTRACT

Conventional fracture-characterization techniques operate with the idealized model of penny-shaped (rotationally invariant) cracks and ignore the roughness (microcorrugation) of fracture surfaces. Here, we develop analytic solutions based on the linear-slip theory to examine wave propagation through an effective triclinic medium that contains two microcorrugated, vertical, orthogonal fracture sets in isotropic background rock.

The compliance matrix off-diagonal elements associated with the corrugation cause the deviation of the polarization vectors of the vertically traveling S-waves from the horizontal plane. Also, the shear-wave splitting coefficient at vertical incidence becomes sensitive to fluid saturation, especially for tight, low-porosity host rock. In contrast to the model with two orthogonal sets of penny-shaped cracks, the NMO (normal-moveout) ellipses of all three reflection modes (P, S_1 , S_2) are rotated with respect to the fracture strike directions. Another unusual property of the fast shear wave S_1 , which can help to distinguish between models with one and two microcorrugated fracture sets, is the misalignment of the semi-major axis of its NMO ellipse and the polarization vector at vertical incidence. The model analyzed here may adequately describe the orthogonal fracture sets at Weyburn Field in Canada, where the axes of the P-wave NMO ellipse deviate from the S_1 -wave polarization direction. Our results can be used to identify the underlying physical model and, potentially, estimate the combinations of fracture parameters constrained by wide-azimuth, multicomponent seismic data.

Key words: fracture characterization, microcorrugated fractures, wide-azimuth data, multicomponent seismic, NMO ellipse, AVO gradient

1 INTRODUCTION

A key element in reservoir characterization is identification of fluid pathways that control the production of hydrocarbons. Since such pathways are often formed by fracture networks and joints, detection and analysis of fractures using seismic data is an important area of reservoir geophysics (e.g. Lynn et al., 1995; Pérez et al., 1999; Mallick et al., 1998; DeVault et al., 2002). In a series of three papers, Bakulin et al. (2000a,b,c) outlined several practical approaches to estimating fracture parameters from surface seismic and VSP (vertical seismic profiling) data. Using the linear-slip theory of Schoenberg (1980), they represented the equations de-

scribing the NMO (normal-moveout) ellipses and AVO (amplitude-variation-with-offset) gradients of reflected waves in terms of fracture compliances and orientations. These analytic expressions helped Bakulin et al. (2000a,b,c) to devise fracture-characterization methods based on the inversion of multicomponent, mutli-azimuth reflection data.

The work of Bakulin et al. (2000a,b,c) was largely focused on the idealized model of rotationally invariant fractures (i.e., oblate spheroids), which have perfectly smooth surfaces and are often called “penny-shaped cracks.” Grechka et al. (2003) extended the results of Bakulin et al. (2000a) by considering a single set of the most general vertical fractures allowed by the linear-

slip formalism. Physically, such “general” fractures have rough (microcorrugated) surfaces and are described by a compliance matrix that has nonzero off-diagonal elements. The results of Grechka et al. (2003) show that fracture rheology has a strong impact on velocities and reflection moveout of pure modes, as well as on the shear-wave splitting coefficient. For instance, if the fractures are rotationally invariant, the axes of the NMO ellipses from horizontal reflection events are always parallel and perpendicular to the fracture strike. By contrast, for a set of general fractures only the NMO ellipse of the fast shear wave S_1 maintains its alignment with the fractures, while the ellipses of the P- and S_2 -waves may have different orientations.

While the methodology of Grechka et al. (2003) helps to treat realistic fracture rheology, their results are limited to effective media that include only one general fracture set. Many naturally fractured reservoirs, however, contain two (or even more) systems of fractures, which are often orthogonal to each other (Schoenberg and Sayers, 1995; Grechka and Tsvankin, 2003). Here, we study the effective triclinic medium formed by two vertical, orthogonal, microcorrugated fracture sets embedded in isotropic background rock.

Our motivation for investigating this model comes from analysis of multicomponent, multiazimuth reflection data acquired at Weyburn Field in Canada. Borehole imaging and geological information reveal the presence of two dominant fracture sets, which are interpreted as approximately orthogonal over most of the field (Cardona, 2002). The assumption that both fracture sets are rotationally invariant cannot explain the misalignment of P-wave NMO ellipses and the fast S-wave polarization direction observed by Cardona (2002) in some parts of the reservoir. Making the fractures microcorrugated can help to develop an effective model that accounts for this anomaly without introducing a third fracture system.

The objective of this paper is to analyze the influence of two orthogonal sets of microcorrugated fractures on the NMO ellipses and AVO gradients of reflected waves, as well as on the shear-wave splitting coefficient. By applying the weak-anisotropy approximation, we derive closed-form analytic expressions for these common seismic signatures in terms of the fracture compliances. Although the feasibility study by Grechka and Tsvankin (2003) indicates that the individual compliances of two general fracture sets cannot be resolved even from the complete effective stiffness tensor, our results can assist in retrieving certain combinations of the compliances and identifying the presence of a second fracture set.

2 EFFECTIVE MODEL

The model considered here includes two orthogonal sets of vertical fractures of the most general rheology embedded in a purely isotropic background (Figure 1). To

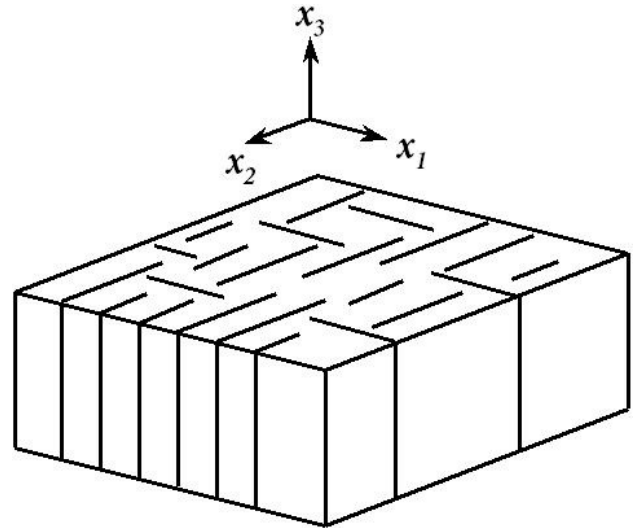


Figure 1. Illustration of a model of two sets of vertical fractures orthogonal to each other in an isotropic background. Since the linear-slip theory does not account for the interaction of fracture sets, fractures are not supposed to intersect each other.

compute the elastic stiffnesses for the fractured model, we employ the linear-slip theory introduced by Schoenberg (1980), Schoenberg and Sayers (1995), and others (see Appendix A). According to the linear-slip formalism, fractures can be described as non-welded interfaces that cause discontinuities in the displacement field (i.e., slips). The slips are proportional to the product of the (continuous) tractions that act across the fractures and to the excess fracture compliances.

The most general mathematical description of a fracture set in the linear-slip theory is a 3×3 symmetric matrix of the excess compliances (Grechka et al., 2003):

$$\mathbf{K} = \begin{pmatrix} K_N & K_{NV} & K_{NH} \\ K_{NV} & K_V & K_{VH} \\ K_{NH} & K_{VH} & K_H \end{pmatrix}, \quad (1)$$

where K_N is the normal compliance responsible for relating the normal traction (stress) across the fracture surface to the normal slip, and K_V and K_H are the tangential compliances that relate the shear stresses to the tangential slips. The off-diagonal compliances incorporate the mechanical effects of irregularities and asperities on the fracture surfaces (Figure 2) by coupling normal slips to shear stresses and vice-versa (Schoenberg and Douma, 1988; Nakagawa et al., 2000).

Fractures are usually classified in accordance with the structure of their compliance matrix \mathbf{K} [equation (1)]. If at least one of the off-diagonal elements does not vanish, the fractures are sometimes called “monoclinic” (Schoenberg and Douma, 1988). Fractures described by a diagonal matrix \mathbf{K} are called “orthotropic”

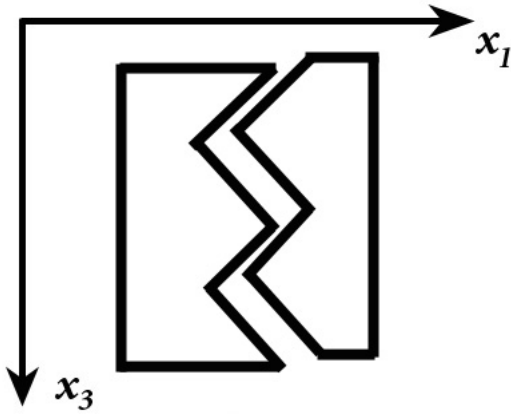


Figure 2. Idealized fracture with corrugations that are off-set from one face to the other (adapted from Schoenberg and Douma, 1988). In such a model, normal slips (discontinuities in displacement) are coupled to shear stresses and vice-versa. For example, the slip in the x_3 -direction will cause the coupling of the fracture faces and, therefore, shear stress in the x_1 -direction.

or simply “diagonal”; rotationally invariant fractures are a special subset of diagonal fractures corresponding to equal tangential compliances $K_V = K_H$.

The stiffness matrix of the effective model is obtained by adding the compliance matrices of the two corrugated fracture sets to that of the isotropic background (Appendix B):

$$\mathbf{c} = \begin{pmatrix} c_{11} & c_{12} & c_{13} & \chi c_{24} & c_{15} & c_{16} \\ c_{12} & c_{22} & c_{23} & c_{24} & \chi c_{15} & c_{26} \\ c_{13} & c_{23} & c_{33} & \chi c_{24} & \chi c_{15} & c_{36} \\ \chi c_{24} & c_{24} & \chi c_{24} & c_{44} & 0 & c_{46} \\ c_{15} & \chi c_{15} & \chi c_{15} & 0 & c_{55} & c_{56} \\ c_{16} & c_{26} & c_{36} & c_{46} & c_{56} & c_{66} \end{pmatrix} \quad (2)$$

where

$$\chi \equiv \frac{\lambda}{(\lambda + 2\mu)}.$$

Equation (2) demonstrates that the effective model has the most general, triclinic symmetry (i.e., it does not have axes of rotational symmetry or symmetry planes), with only one vanishing elastic constant, $c_{45} = c_{54}$. This is not surprising since even a single set of microcorrugated fractures creates an effective triclinic medium. Nonetheless, only 14 out of the 20 elastic constants are independent because the effective model is constructed using two Lamé parameters of the isotropic background (λ and μ) and 12 fracture compliances (six for each fracture set). Note that if the fracture azimuth is unknown, it is also necessary to introduce an orientation angle that defines the azimuth of one of the sets in our coordinate frame.

By dividing the matrix \mathbf{c} into 3×3 submatrices

\mathbf{C}_{MN} , it can be represented in block form:

$$\mathbf{c} = \begin{pmatrix} \mathbf{C}_{NN} & \mathbf{C}_{NT} \\ \mathbf{C}_{NT}^T & \mathbf{C}_{TT} \end{pmatrix}, \quad (3)$$

The influence of the complex fracture rheology in our model on the structure of the stiffness matrix can be understood by comparing the matrix (3) with that for the effective orthorhombic medium due to two orthogonal sets of *rotationally invariant* fractures (Bakulin et al., 2000b):

$$\mathbf{c}^{\text{orth}} = \begin{pmatrix} \mathbf{C}_{NN}^{\text{orth}} & \mathbf{0} \\ \mathbf{0} & \mathbf{C}_{TT}^{\text{orth}} \end{pmatrix}. \quad (4)$$

Here, the matrix $\mathbf{C}_{TT}^{\text{orth}}$ is diagonal, and c_{66} contained in $\mathbf{C}_{TT}^{\text{orth}}$ is a linear combination of c_{44} and c_{55} .

The expressions for the effective stiffness elements c_{ij} in equation (2) can be simplified by linearizing the exact results in the normalized compliances which are called *fracture weaknesses* (Bakulin et al., 2000a). The weaknesses vary from zero for unfractured medium to unity for intensely fractured rock in which the body-wave velocities go to zero in a certain direction. Since the weaknesses for typical fractured formations are much smaller than unity, they can be conveniently used in developing linearized approximations for seismic signatures. Definitions of the fracture weaknesses are given in Appendix B, as well as the resulting linearized c_{ij} elements.

3 VERTICAL WAVE PROPAGATION

The phase velocities and polarization vectors of vertically propagating plane waves can be obtained by solving the Christoffel equation for the effective medium described by the stiffness matrix (2). Applying the first-order perturbation theory (e.g., Jech and Pšenčík, 1989; Pšenčík and Vavryčuk, 2002) yields the following simplified expressions for the vertical velocities of the P-, S_{1-} , and S_{2-} waves:

$$V_P \approx V_{Pb} \left[1 - \frac{1}{2} (\Delta_{N_1} + \Delta_{N_2}) \chi^2 \right], \quad (5)$$

$$V_{S1} \approx V_{Sb} \left(1 - \frac{\Delta_{V_2}}{2} \right), \quad (6)$$

$$V_{S2} \approx V_{Sb} \left(1 - \frac{\Delta_{V_1}}{2} \right), \quad (7)$$

where V_{Pb} and V_{Sb} are the P- and S-wave velocities in the isotropic background, whereas Δ_{N_i} and Δ_{V_i} correspond to the normal and vertical weaknesses of fracture sets 1 and 2, as indicated by the index i . Although the vertical velocities are influenced by the presence of fractures, equations (5)–(7) do not contain off-diagonal weaknesses and coincide with the linearized velocities for rotationally invariant fractures (Bakulin et al. (2000b)).

In contrast, the body waves polarization vectors (\mathbf{U}_m), contain first-order contributions of the off-diagonal compliances Δ_{NV_i} :

$$\mathbf{U}_P \approx (a \Delta_{NV_1}, a \Delta_{NV_2}, 1)^T, \quad (8)$$

$$\mathbf{U}_{S1} \approx (0, 1, -a \Delta_{NV_2})^T, \quad (9)$$

$$\mathbf{U}_{S2} \approx (1, 0, -a \Delta_{NV_1})^T, \quad (10)$$

where

$$a \equiv \frac{(1 - 2g_b)}{(1 - g_b)} \sqrt{g_b}, \quad g_b \equiv \left(\frac{V_{Sb}}{V_{Pb}} \right)^2.$$

Because of the corrugation of fracture surfaces, the P-wave polarization vector deviates from the vertical, and the vertically propagating shear waves are no longer polarized in the horizontal plane. Equations (9) and (10), however, show that the shear-wave polarization vectors are still confined to the planes of the two fracture sets.*

Therefore, Alford-style rotation of the horizontal displacement components of near-offset S-wave reflections can be used to estimate the fracture azimuths. To measure the vertical components of the shear-wave polarization vectors, which are indicative of the presence of microcorrugated fractures, it is necessary to apply 3D polarization analysis.

3.1 Shear-wave splitting

The shear-wave splitting coefficient (γ^S) at vertical incidence is defined as (Thomsen, 1988; Tsvankin, 2001)

$$\gamma^S \equiv \frac{V_{S1}^2 - V_{S2}^2}{2V_{S2}^2}, \quad (11)$$

where V_{S1} is the velocity of the fast shear wave. Applying the second-order perturbation theory (Farra, 2001) in terms of the fracture weaknesses yields

$$\gamma^S \approx \frac{1}{2} \left\{ (\Delta_{V_1} - \Delta_{V_2})(1 + \Delta_{V_1} - \Delta_{V_2}) - g_b \left[(\Delta_{V_{H_1}}^2 - \Delta_{V_{H_2}}^2) + (\Delta_{NV_1}^2 - \Delta_{NV_2}^2) \frac{(3 - 4g_b)}{1 + g_b} \right] \right\} \quad (12)$$

As expected, γ^S at vertical incidence vanishes when the two fracture sets are identical. If the terms quadratic in the weaknesses are dropped from equation (12), the splitting coefficient reduces to the difference between the diagonal tangential weaknesses Δ_{V_1} and Δ_{V_2} [see

*Due to the limitations of the first-order perturbation theory, the shear-wave polarization vectors are no longer orthogonal, despite being perpendicular to the P-wave polarization vector. Also, the perturbed polarization vectors were not normalized; still, to the first order in the fracture weaknesses, the magnitude of the vectors \mathbf{U}_P , \mathbf{U}_{S1} and \mathbf{U}_{S2} is equal to unity.

equations (9) and (10)]. Therefore, to the first order γ^S coincides with the splitting coefficient for rotationally invariant fractures, which is controlled by the difference between the fracture densities of the two sets (Thomsen (1988); Bakulin et al. (2000a,b)).

However, if the second-order terms are substantial, γ^S is also influenced by the off-diagonal weaknesses $\Delta_{V_{H_i}}$ and Δ_{NV_i} . Note that the weakness Δ_{NV_i} depends on saturation and takes different values for fractures filled with compressible gas, brine, or oil (Bakulin et al. (2000c)).[†] Therefore, the vertical-incidence splitting coefficient for microcorrugated fractures with relatively large off-diagonal weaknesses may serve as an indicator of fluid saturation.

As illustrated by Figure 3, the exact coefficient γ^S can vary by as much as 50% over the entire range of plausible values of Δ_{NV_1} (Δ_{NV_2} was fixed). For a tight (non-porous) host rock, $\Delta_{NV_1} = 0$ corresponds to fractures filled with incompressible fluid such as brine, whereas nonzero values of Δ_{NV_1} describe fractures at least partially saturated with gas (Bakulin et al., 2000c). Although the weak-anisotropy approximation (12) correctly reproduces the overall character of the curve $\gamma^S(\Delta_{NV_1})$, it underestimates the sensitivity of the shear splitting to the weakness Δ_{NV_1} .

If the saturation of both fracture sets changes simultaneously and Δ_{NV_2} varies similarly to Δ_{NV_1} , the splitting coefficient becomes less sensitive to fluid content. Also, when the host rock has pore space hydraulically connected to the fractures, the weaknesses Δ_{NV_i} do not necessarily vanish even for incompressible saturating fluids (Cardona, 2002; Gurevich, 2003). As a consequence, for porous rocks the variation of γ^S with saturation may be less pronounced than that suggested by Figure 3. Finally, γ^S becomes less sensitive to the off-diagonal compliances and saturation for softer rocks (e.g., marine sediments) with smaller values of the ratio g_b .

4 NMO ELLIPSES FOR HORIZONTAL REFLECTORS

Important information for fracture detection is provided by azimuthally varying traveltimes (moveout) of reflected waves, in particular by their normal-moveout (NMO) ellipses. For a horizontal, homogeneous layer of arbitrary anisotropic symmetry, the NMO velocity of pure (non-converted) reflection modes as a function of the azimuth α is given by (Grechka et al., 1999):

$$V_{\text{nmo}}^{-2} = W_{11} \cos^2 \alpha + 2W_{12} \sin \alpha \cos \alpha + W_{22} \sin^2 \alpha, \quad (13)$$

[†]Equation (12) is more accurate than equation (30) of Bakulin et al. (2000c) because it includes terms quadratic in the weaknesses.

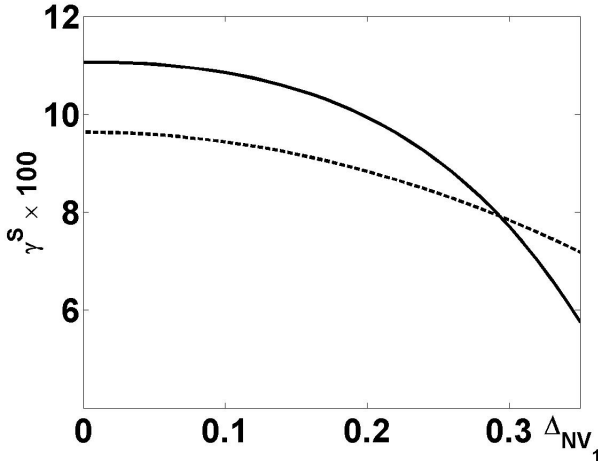


Figure 3. Variation of the shear-wave splitting coefficient (γ^S) for vertical propagation as a function of the weakness Δ_{NV_1} . The solid line is the exact γ^S from equation (11), where the velocities are computed from the Christoffel equation; the dashed curve is the approximation (12). The model parameters are $V_{Pb} = 3$ km/s, $V_{Sb} = 1.5$ km/s, $\Delta_{N_1} = 0.5$, $\Delta_{V_1} = \Delta_{H_1} = 0.25$ and $\Delta_{NH_1} = \Delta_{VH_1} = 0.1$. Each weakness of the second fracture set except for Δ_{NV_2} is equal one-third of the corresponding weakness of the first set; $\Delta_{NV_2} = 1/3\Delta_{NH_1}$.

where \mathbf{W} is a symmetric 2×2 matrix:

$$\mathbf{W} = \frac{q}{q_{,12}^2 - q_{,11}q_{,22}} \begin{pmatrix} q_{,22} & -q_{,12} \\ -q_{,12} & q_{,11} \end{pmatrix}. \quad (14)$$

Here, q is the vertical component of the slowness vector $\mathbf{p} = [p_1, p_2, q]$ of the zero-offset ray and $q_{,ij}$ denote the following partial derivatives evaluated at zero offset:

$$q_{,ij} \equiv \frac{\partial^2 q(p_1, p_2)}{\partial p_i \partial p_j}. \quad (15)$$

The vertical slowness and its derivatives can be obtained from the Christoffel equation, as discussed by Grechka et al. (1999). If the eigenvalues of the matrix \mathbf{W} are positive (the most typical case), equation (13) describes an ellipse in the horizontal plane.

To analyze the dependence of the NMO ellipses on the medium parameters, it is convenient to linearize equation (14) in the fracture weaknesses [equations (B1)–(B6)]. For P-waves, the linearized matrix \mathbf{W} takes the form

$$\mathbf{W}^P \approx \frac{1}{V_{Pb}^2} \begin{pmatrix} W_{11}^P & W_{12}^P \\ W_{12}^P & W_{22}^P \end{pmatrix}, \quad (16)$$

where

$$W_{11}^P = 1 + \Delta_{N_1} (1 - 4g_b^2) + \Delta_{N_2} (1 - 2g_b)^2 + 4g_b \Delta_{V_1}, \quad (17)$$

$$W_{12}^P = 2(\Delta_{NH_1} + \Delta_{NH_2})(1 - 2g_b)\sqrt{g_b}, \quad (18)$$

$$W_{22}^P = 1 + \Delta_{N_2} (1 - 4g_b^2) + \Delta_{N_1} (1 - 2g_b)^2 + 4g_b \Delta_{V_2}. \quad (19)$$

The structure of equations (17)–(19) can be understood from the ‘‘addition rule’’ formulated by Bakulin et al. (2000b). To find the linearized weak-anisotropy approximation for most seismic signatures (one exception is discussed below), the anisotropic terms due to each fracture set can be simply added together taking into account the fracture orientation. This recipe can be used to obtain equations (17)–(19) from the P-wave NMO ellipse for a single set of microcorrugated fractures given in equation (56) of Grechka et al. (2003).

For the fast shear wave S_1 the matrix \mathbf{W} becomes

$$\mathbf{W}^{S_1} \approx \frac{1}{V_{Sb}^2} \begin{pmatrix} W_{11}^{S_1} & W_{12}^{S_1} \\ W_{12}^{S_1} & W_{22}^{S_1} \end{pmatrix}, \quad (20)$$

with

$$W_{11}^{S_1} = 1 + \Delta_{H_1} + \Delta_{H_2} - \mathcal{A}, \quad (21)$$

$$W_{12}^{S_1} = \sqrt{g_b} (2\Delta_{NH_2} - \mathcal{C}), \quad (22)$$

$$W_{22}^{S_1} = 1 - 3\Delta_{V_2} + 4g_b \Delta_{N_2} - \mathcal{B}. \quad (23)$$

Here,

$$\mathcal{A} \equiv \mathcal{D} \Delta_{VH_1}^2, \quad (24)$$

$$\mathcal{B} \equiv \mathcal{D} \Delta_{VH_2}^2, \quad (25)$$

$$\mathcal{C} \equiv \mathcal{D} \Delta_{VH_1} \Delta_{VH_2}, \quad (26)$$

$$\mathcal{D} \equiv \frac{g_b}{(\Delta_{V_1} - \Delta_{V_2})}. \quad (27)$$

Although the factors \mathcal{A} , \mathcal{B} , and \mathcal{C} are proportional to products of the weaknesses Δ_{VH_i} , their denominator contains the difference in the tangential weaknesses Δ_{V_i} [see equation (27)]. For that reason, \mathcal{A} , \mathcal{B} , and \mathcal{C} have to be retained in the linearized approximation for the NMO ellipse \mathbf{W}^{S_1} . In such a case, the addition rule discussed above is not valid, and the approximate NMO ellipse of the S_1 -wave cannot be obtained as the sum of the contributions of each fracture set.

The linearized matrix \mathbf{W} for the S_2 -wave is given by

$$\mathbf{W}^{S_2} \approx \frac{1}{V_{Sb}^2} \begin{pmatrix} W_{11}^{S_2} & W_{12}^{S_2} \\ W_{12}^{S_2} & W_{22}^{S_2} \end{pmatrix}, \quad (28)$$

where

$$W_{11}^{S_2} = 1 - 3\Delta_{V_1} + 4g_b \Delta_{N_1} + \mathcal{A}, \quad (29)$$

$$W_{12}^{S_2} = \sqrt{g_b} (2\Delta_{NH_1} + \mathcal{C}), \quad (30)$$

$$W_{22}^{S_2} = 1 + \Delta_{H_1} + \Delta_{H_2} + \mathcal{B}. \quad (31)$$

Equations (16)–(31) show that only the presence of the off-diagonal weaknesses can explain the misalignment of the NMO ellipses with the fracture planes. If both fracture sets were rotationally invariant, the matrices \mathbf{W} for all three modes [equations (16), (20), and (28)] would be diagonal, and the axes of the NMO

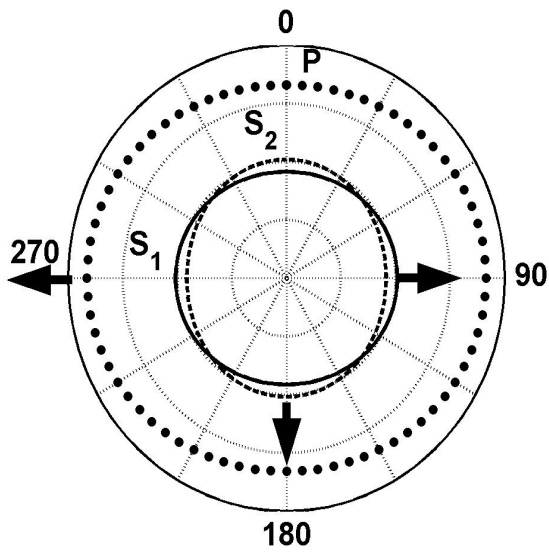


Figure 4. Exact NMO ellipses for an effective orthorhombic model formed by two vertical, orthogonal sets of rotationally invariant fractures. The semi-major axes (black arrows) of the P- and S₁-wave NMO ellipses are parallel to the strike of the dominant fractured set (azimuth 90°). The parameters are $V_{Pb} = 2$ km/s, $V_{Sb} = 1$ km/s, $\Delta_{N_1} = 0.25$, and $\Delta_{V_1} = \Delta_{H_1} = 0.12$. Each weakness of the second fracture set is equal to one-third of the corresponding weakness of the first set. The radius of the external circle corresponds to 2 km/s.

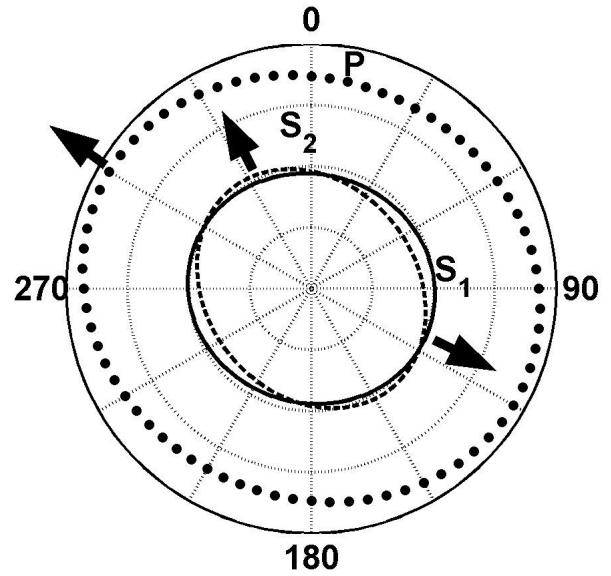


Figure 5. Exact NMO ellipses for two vertical, orthogonal sets of microcorrugated fractures. The strike azimuth of the dominant fracture set is 90°. The parameters are $V_{Pb} = 2$ km/s, $V_{Sb} = 1$ km/s, $\Delta_{N_1} = 0.25$, $\Delta_{V_1} = \Delta_{H_1} = 0.12$, $\Delta_{NV_1} = \Delta_{NH_1} = 0.17$, and $\Delta_{VH_1} = 0.12$. Each weakness of the second fracture set is equal to one-third of the corresponding weakness of the first set.

ellipses would be parallel to the fracture strike directions. In an effective orthorhombic medium due to two orthogonal sets of rotationally invariant fractures, the semi-major axes of the NMO ellipses of the P- and S₁-waves (see Figure 4) are aligned with the strike of the dominant fracture set (Bakulin et al., 2000b).

By contrast, when both fracture sets are microcorrugated, all three NMO ellipses generally have different orientations, and none of them is aligned with the fracture azimuths (Figure 5). The deviation of the semi-major axis of the NMO ellipse from the azimuth of the dominant fracture sets reaches 40° for the S₂-wave, 30° for the P-wave and 20° for the S₁-wave. The weak-anisotropy approximations for the NMO ellipses are close to the exact solutions for the full range of azimuths (Figure 6). The error of the approximate solution, caused primarily by the misalignment of the axes of the exact and approximate NMO ellipses, is noticeable only for the slow wave S₂. The higher accuracy of the approximation for the S₁-wave compared to that for the S₂-wave is not surprising since equations (22) and (23) for the matrix elements $W_{12}^{S_1}$ and $W_{22}^{S_1}$ become exact for one set of fractures (Grechka et al., 2003).

The orientation of the NMO ellipse of the fast wave S₁ can help to distinguish between the models with one or two microcorrugated fracture sets. If the second set does not exist, then $\Delta_{NH_2} = \Delta_{VH_2} = 0$, and the

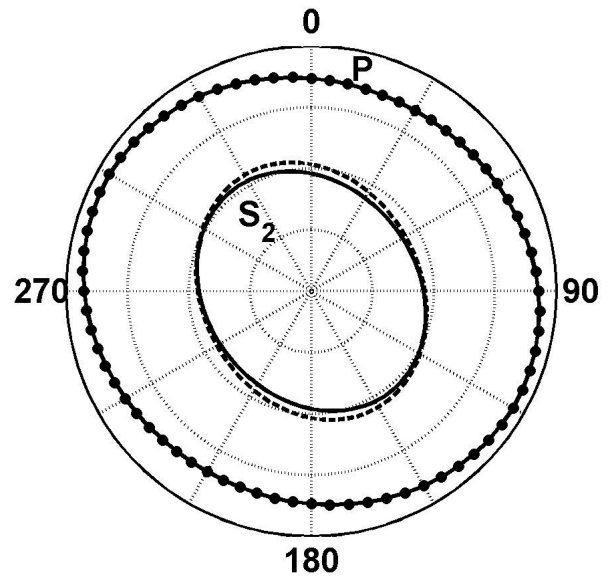


Figure 6. Comparison between the exact NMO ellipses of the P- and S₂-waves from Figure 5 (solid lines) and the weak-anisotropy approximations (dots for the P-wave and the dashed line for the S₂-wave). The approximations are computed from equations (17)–(19) and (29)–(31). The exact and approximate NMO ellipses of the S₁-wave (not shown) practically coincide with each other.

element W_{12} for the S_1 -wave vanishes [equations (22) and (26)]. In this case, the matrix \mathbf{W}^{S_1} [equation (20)] becomes diagonal, and the semi-major axis of the NMO ellipse of the S_1 -wave is parallel to both the fast shear-wave polarization direction [equation (9)] and the fracture strike. Moreover, for the model with one set of microcorrugated fractures, the S_1 -wave vertical velocity coincides with the NMO velocity in the fracture strike direction. This result, discussed by Grechka et al. (2003), follows from equations (6) and (20).

Grechka et al. (2000) defined the Thomsen-style parameters $\zeta^{(i)}$ ($i = 1, 2, 3$) responsible for the orientations of the NMO ellipses of pure modes in a horizontal monoclinic layer with a horizontal symmetry plane. Equations (16)–(31) can be used to generalize their result for our triclinic model because the elements W_{12} include the parameters $\zeta^{(i)}$ and additional correction terms for the shear waves. Using equations (B21) and (B24), the element W_{12}^P [equation (18)] responsible for the rotation of the P-wave NMO ellipse with respect to the x_1 -axis can be represented as

$$W_{12}^P = -2 \frac{c_{36}}{c_{33}} = -2\zeta^{(3)}, \quad (32)$$

which coincides with the expression for W_{12}^P in Grechka et al. (2000). For our model, the parameter $\zeta^{(3)}$ is proportional to the sum of the weaknesses Δ_{NH_1} and Δ_{NH_2} .

Similarly, the off-diagonal elements $W_{12}^{S_1}$ and $W_{12}^{S_2}$ for shear waves [equations (22) and (30)] can be expressed through the parameters $\zeta^{(1)}$ and $\zeta^{(2)}$:

$$W_{12}^{S_1} = -2 \frac{c_{16} - c_{36}}{2V_{Pb}^2 g_b} + \mathcal{C} = -2 \frac{\zeta^{(1)}}{g_b} + \mathcal{C}, \quad (33)$$

$$W_{12}^{S_2} = -2 \frac{c_{26} - c_{36}}{2V_{Pb}^2 g_b} - \mathcal{C} = -2 \frac{\zeta^{(2)}}{g_b} - \mathcal{C}, \quad (34)$$

where \mathcal{C} ($\Delta_{V_i}, \Delta_{V_{H_i}}$) [equation (26)] is an additional correction factor that accounts for the nonzero stiffnesses c_{46} and c_{56} in the triclinic model [equation (3)]. The parameters $\zeta^{(1)}$ and $\zeta^{(2)}$ depend on the weaknesses Δ_{NH_2} and Δ_{NH_1} , respectively.

Our approximations for the NMO ellipse of both S-waves break down when tangential weaknesses Δ_{V_1} and Δ_{V_2} are identical and the weaknesses $\Delta_{V_{H_i}} \neq 0$. In this case, the parameter \mathcal{D} [equation (27)] goes to infinity, which reflects the fact that a point shear-wave singularity develops in a close vicinity of the zero-offset ray. An analysis of the influence of singularities on normal moveout for models with orthogonal sets of penny-shaped cracks can be found in Bakulin et al. (2000b).

5 P-WAVE REFLECTION COEFFICIENT

Another seismic signature that can be effectively used in fracture detection is the azimuthally varying reflection coefficient, in particular the AVO (amplitude variation with offset) gradient responsible for small- and

moderate-offset reflection amplitudes. Here, we present a linearized expression for the P-wave AVO response in our model and discuss its dependence on the fracture weaknesses.

We consider an isotropic incidence halfspace above the triclinic medium described by equation (2) and assume a weak contrast in the elastic properties across the interface and weak anisotropy (i.e., small fracture weaknesses) in the reflecting halfspace. The weak-contrast, weak-anisotropy approximation for the P-wave reflection coefficient in arbitrary anisotropic media is derived in Vavryčuk and Pšenčík (1998). By combining their general result with the linearized stiffness coefficients for our model [equations (B10)–(B30)], we find the P-wave reflection coefficient R_{PP} as a function of the phase incidence angle θ :

$$\begin{aligned} R_{PP} &= A + B \sin^2 \theta + C \sin^2 \theta \tan^2 \theta \\ &= A_{\text{iso}} + (B_{\text{iso}} + B_{\text{ani}}) \sin^2 \theta \\ &\quad + (C_{\text{iso}} + C_{\text{ani}}) \sin^2 \theta \tan^2 \theta. \end{aligned} \quad (35)$$

Here, $A = A_{\text{iso}}$ is the normal-incidence reflection coefficient that is not influenced by anisotropy, B is the AVO gradient, and C is the so-called ‘‘curvature’’ (large-angle) term. Both B and C can be separated into the isotropic (subscript ‘‘iso’’) and anisotropic (subscript ‘‘ani’’) parts, with the anisotropic part of the AVO gradient given by

$$\begin{aligned} B_{\text{ani}}(\phi) &= g_b \left\{ -[(1 - 2g_b) \Delta_{N_1} + \Delta_{V_1}] \cos^2 \phi \right. \\ &\quad - \frac{1}{2\sqrt{g_b}} (\Delta_{NH_1} + \Delta_{NH_2}) (1 - 2g_b) \sin 2\phi \\ &\quad \left. + [\Delta_{V_2} - 2\Delta_{V_1} - (1 - 2g_b) \Delta_{N_2}] \sin^2 \phi \right\}, \end{aligned} \quad (36)$$

where ϕ is the azimuthal phase angle measured from the x_1 -axis. The anisotropic curvature term is expressed as

$$\begin{aligned} C_{\text{ani}}(\phi) &= -g_b \left\{ (\Delta_{N_1} \cos^4 \phi + \Delta_{N_2} \sin^4 \phi) (1 - g_b) \right. \\ &\quad + \frac{1}{2\sqrt{g_b}} \left[(\Delta_{NH_1} + \Delta_{NH_2} (1 - 2g_b)) \cos^2 \phi \right. \\ &\quad + \frac{1}{2} (\Delta_{H_1} + \Delta_{H_2} + (\Delta_{N_1} + \Delta_{N_2}) (1 - 2g_b)) \sin 2\phi \\ &\quad \left. \left. + (\Delta_{NH_1} (1 - 2g_b) + \Delta_{NH_2}) \sin^2 \phi \right] \sin 2\phi \right\}. \end{aligned} \quad (37)$$

There are similarities between equations (36) and (37) and equations (16)–(19) for the P-wave NMO ellipse. First, $B_{\text{ani}}(\phi)$ traces out a curve close to an ellipse in the horizontal plane, with $B_{\text{ani}}^{-2}(\phi)$ being exactly elliptical. Second, the only off-diagonal weaknesses appearing in the linearized equations for both the reflection coefficient and NMO ellipse are Δ_{NH_1} and Δ_{NH_2} . Third, the ‘‘principal direction’’ of the curve $B_{\text{ani}}(\phi)$

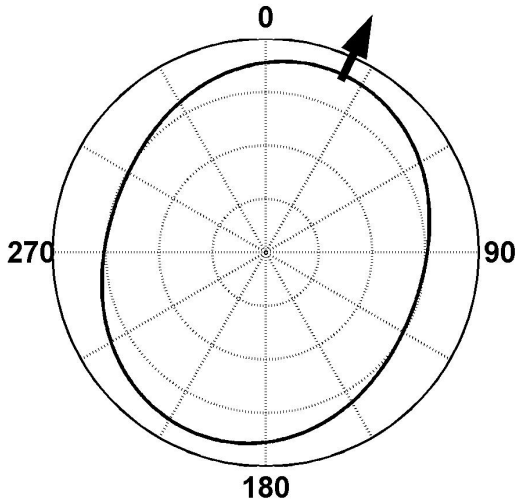


Figure 7. Azimuthal variation of the P-wave AVO gradient for our triclinic model computed from equation (36). The strike azimuth of the dominant fracture set is 90° ; the direction of the largest gradient (black arrow) is close to 65° . The parameters are $V_{Pb}/V_{Sb} = 3$, $\Delta_{NH_1} = 0.25$, $\Delta_{V_1} = \Delta_{H_1} = 0.12$, and $\Delta_{NH_1} = 0.05$. Each weakness of the second fracture set is equal to one-third of the corresponding weakness of the first set.

is rotated with respect to the horizontal coordinate axes (i.e., with respect to the fracture azimuths) only when $\Delta_{NH_1} \neq 0$ or $\Delta_{NH_2} \neq 0$. Furthermore, the rotation angle of both the NMO ellipse [equation (18)] and AVO gradient [equation (36)] is controlled by the sum $\Delta_{NH_1} + \Delta_{NH_2}$. As shown above, the rotation angle can be also expressed through the anisotropy coefficient $\zeta^{(3)}$ [equation (32)].

The example in Figure 7 illustrates the orientation and shape of the AVO gradient from equation (36). The curve $B_{\text{ani}}(\phi)$ is close to an ellipse with the semi-major axis deviating by about 65° from the strike of the dominant fracture set. If the weaknesses Δ_{NH_1} and Δ_{NH_2} are set to zero, the direction of the largest (by absolute value) AVO gradient is perpendicular to the dominant fracture set. Despite the small value of $\Delta_{NH_1} = 0.05$, the contribution of the off-diagonal weaknesses is sufficient for rotating this direction by about 25° .

6 DISCUSSION AND CONCLUSIONS

We studied seismic signatures of an effective medium formed by two sets of vertical, orthogonal fractures with microcorrugated surfaces embedded in isotropic host rock. Each fracture set is described by the most general compliance matrix allowed within the framework of the linear-slip theory, with the off-diagonal compliance elements responsible for the character and degree of corrugation. The effective model is triclinic and has

no symmetry planes, although only 14 stiffness elements are independent.

By applying expansions in the fracture weaknesses (normalized compliances), we derived closed-form analytic expressions for shear-wave splitting, the NMO ellipses of horizontal reflection events, and the P-wave reflection coefficient. These weak-anisotropy approximations provide valuable insight into the influence of the fracture rheology on seismic signatures commonly used in reservoir characterization. For instance, the presence of the off-diagonal compliances makes the shear-wave splitting coefficient γ^S at vertical incidence sensitive (to the second order) to fluid saturation. The variation of γ^S with saturation may be substantial in tight, high-velocity formations where fluids cannot easily move from the fractures into pore space.

The fracture compliances also control the orientation and eccentricity of the NMO ellipses of the reflected P-, S_1 -, and S_2 -waves. In particular, the contributions of the off-diagonal compliances Δ_{NH_i} and Δ_{VH_i} ($i = 1, 2$) lead to the rotation of the NMO ellipses with respect to the fracture strike directions. In contrast to the effective orthorhombic medium formed by two orthogonal sets of penny-shaped cracks, all three NMO ellipses in our model have different orientations. Extending the results of Grechka et al. (2000) for monoclinic models, we expressed the rotation angles of the NMO ellipses in triclinic media through the anisotropy parameters $\zeta^{(1)}$, $\zeta^{(2)}$, and $\zeta^{(3)}$.

Analysis of the NMO ellipse of the fast shear wave S_1 suggests a simple way to distinguish between models with one and two microcorrugated fracture sets. For a single set of fractures, the semi-major axis of the S_1 -wave NMO ellipse and the polarization vector of the S_1 -wave at vertical incidence are parallel to each other and to the fracture strike. This is no longer the case for the model with two fracture sets where the angle between the polarization vector and the semi-major axis of the NMO ellipse for the S_1 -wave can reach 20 – 30° .

For P-waves, the principal azimuthal directions of both the NMO ellipse and AVO gradient depend on the sum of the off-diagonal weaknesses Δ_{NH_1} and Δ_{NH_2} . If both Δ_{NH_1} and Δ_{NH_2} vanish, then the NMO ellipse and AVO gradient are aligned with the fracture strike directions, as is always the case for penny-shaped cracks. Whereas the azimuthally varying P-wave AVO gradient typically traces out a quasi-elliptical curve, the large-angle AVO term has a much more complicated azimuthal dependence.

The results of this work can be instrumental in developing inversion algorithms for estimating the fracture parameters from multicomponent seismic data. As demonstrated by Grechka and Tsvankin (2003), the inversion for all 14 independent parameters of this model is ill-posed. Even if all 21 elastic constants of the triclinic medium are recovered with high accuracy, it is impossible to resolve the fracture weaknesses individually. The

equations presented here, however, can help to estimate certain parameter combinations and verify whether the underlying physical model is appropriate.

As discussed above, comparison of the NMO ellipse and polarization directions of the S_1 -wave makes it possible to discriminate between the effective models with one and two sets of microcorrugated fractures. Generalizing the results of Bakulin et al. (2000b) and Grechka et al. (2003), it may be possible to invert seismic data for the velocity ratio g_b and the differences between the diagonal weaknesses Δ_{N_i} , Δ_{V_i} and Δ_{H_i} of the two sets, if the vertical velocities are available. Also, the P-wave ellipses and AVO gradient can potentially constrain the sum of weaknesses Δ_{NH_i} .

The weaknesses Δ_{NV_i} do not appear in the linearized equations for any of the NMO ellipses or the P-wave AVO gradient and contribute only to the second-order term in the shear-wave splitting coefficient. The only quantities that contain first-order contributions of Δ_{NV_i} are the vertical components of the S-wave polarization vectors, which may be difficult to measure on field data. Likewise, the weaknesses Δ_{VH_i} are contained only in relatively small terms in the equations for the shear-wave NMO ellipses and for the splitting coefficient γ^S . Therefore, estimation of the weaknesses Δ_{VH_i} and Δ_{NV_i} is likely to be unstable. As pointed out by Grechka et al. (2003), both Δ_{VH} and Δ_{NV} for a single fracture set can be obtained from VSP data using the slowness surface of P-waves. It is not clear, however, if such an algorithm can be extended to the more complicated model treated here.

7 ACKNOWLEDGEMENTS

We are grateful to members of the A(nisotropy)-team of the Center for Wave Phenomena (CWP) at Colorado School of Mines (CSM) for helpful discussions and to Tom Davis, Ken Larner, John Stockwell and Ivan Vasconcelos (all from CSM) for their reviews of the manuscript. Rodrigo Fuck's graduate studies at CSM were funded by CAPES under the scholarship BEX1340-0/00. This work was also supported by the Consortium Project on Seismic Inverse Methods for Complex Structures at CWP and by the Chemical Sciences, Geosciences and Biosciences Division, Office of Basic Energy Sciences, U.S. Department of Energy.

REFERENCES

- Bakulin, A., Grechka, V., and Tsvankin, I., 2000a, Estimation of fracture parameters from reflection seismic data - Part I: HTI model due to a single fracture set: *Geophysics*, **65**, 1788–1802.
- , 2000b, Estimation of fracture parameters from reflection seismic data - Part II: Fractured models with orthorhombic symmetry: *Geophysics*, **65**, 1803–1817.
- , 2000c, Estimation of fracture parameters from reflection seismic data - Part III: Fractured models with monoclinic symmetry: *Geophysics*, **65**, 1818–1830.
- Cardona, R., 2002, Fluid substitution theories and multicomponent seismic characterization of fractured reservoirs: Ph.D. thesis, Colorado School of Mines.
- DeVault, B., Davis, T. L., Tsvankin, I., Verm, R., and Hilterman, F., 2002, Multicomponent AVO analysis, Vacuum field, New Mexico: *Geophysics*, **67**, 701–710.
- Farra, V., 2001, High-order perturbations of the phase velocity and polarization of qP and qS waves in anisotropic media: *Geophysical Journal International*, **147**, 93–104.
- Grechka, V., Bakulin, A., and Tsvankin, I., 2003, Seismic characterization of vertical fractures described as general linear-slip interfaces: *Geophysical Prospecting*, **51**, 117–129.
- Grechka, V., Contreras, P., and Tsvankin, I., 2000, Inversion of normal moveout for monoclinic media: *Geophysical Prospecting*, **48**, 577–602.
- Grechka, V., and Tsvankin, I., 2003, Feasibility of seismic characterization of multiple sets: *Geophysics*, **68**, 1399–1407.
- Grechka, V., Tsvankin, I., and Cohen, J. K., 1999, Generalized Dix equation and analytic treatment of normal-moveout velocity for anisotropic media: *Geophysical Prospecting*, **47**, 117–148.
- Gurevich, B., 2003, Elastic properties of saturated porous rocks with aligned fractures: *Journal of Applied Geophysics*, **54**, 203–218.
- Hood, J. A., 1991, A simple method for decomposing fracture-induced anisotropy: *Geophysics*, **56**, 1275–1279.
- Jech, J., and Pšenčík, I., 1989, First-order perturbation method for anisotropic media: *Geophysical Journal International*, **99**, 369–376.
- Lynn, H., Simon, K. M., Layman, M., Schneider, R., Bates, C. R., and Jones, M., 1995, Use of anisotropy in P-wave and S-wave data for fracture characterization in a naturally fractured gas reservoir: *The Leading Edge*, **14**, 887–893.
- Mallick, S., Craft, K. L., Meister, L. J., and Chambers, R. E., 1998, Determination of the principal directions of azimuthal anisotropy from P-wave seismic data: *Geophysics*, **63**, 692–706.
- Nakagawa, S., Nihei, K. T., and Myer, L. R., 2000, Shear-induced conversion of seismic waves across single fractures: *International Journal of Rock Mechanics and Mining Sciences*, **37**, 203–218.
- Pérez, M. A., Grechka, V., and Michelena, R. J., 1999, Fracture detection in a carbonate reservoir using a variety of seismic methods: *Geophysics*, **64**, 1266–1276.
- Pšenčík, I., and Vavryčuk, V., 2002, Approximate relation between the ray vector and the wave normal in weakly anisotropic media: *Studia Geophysica et Geodaetica*, **46**, 793–807.
- Schoenberg, M., 1980, Elastic wave behavior across lin-

ear slip interfaces: Journal of Acoustical Society of America, **68**, 1516–1521.

Schoenberg, M., and Douma, J., 1988, Elastic wave propagation in media with parallel fractures and aligned cracks: Geophysical Prospecting, **36**, 571–590.

Schoenberg, M., and Muir, F., 1989, A calculus for finely layered anisotropic media: Geophysics, **54**, 581–589.

Schoenberg, M., and Sayers, C. M., 1995, Seismic anisotropy of fractured rock: Geophysics, **60**, 204–211.

Thomsen, L., 1988, Reflection seismology over azimuthally anisotropic media: Geophysics, **53**, 304–313.

Tsvankin, I., 2001, Seismic signatures and analysis of reflection data in anisotropic media: Elsevier Science, Inc.

Vavryčuk, V., and Pšenčík, I., 1998, PP-wave reflection coefficients in weakly anisotropic elastic media: Geophysics, **63**, 2129–2141.

APPENDIX A: OVERVIEW OF THE LINEAR-SLIP THEORY

The linear-slip theory (Schoenberg, 1980; Schoenberg and Sayers, 1995) is designed to find an equivalent (long-wavelength) representation of a medium that contains one or several fracture sets. Fractures are treated as planar and parallel surfaces of weakness, and it is assumed that interaction between fractures can be ignored. The fracture length is taken to be infinite, while fracture apertures have to be small compared to the dominant seismic wavelength. According to the linear-slip theory, the jumps in the displacement vector $[u_i]$ (i.e., “slips”) across a fracture are to the first order proportional to the (continuous) stresses σ_{jk} :

$$[u_i] = hK_{ij}\sigma_{jk}n_k, \quad (\text{A1})$$

where \mathbf{n} is the normal to the fracture plane, h is the average spacing between fractures, and K_{ij} are called the “compliances” of the fracture set. The effective compliance tensor \mathbf{s} of a fractured medium is then found as the sum of the background compliance \mathbf{s}_b and the excess compliances \mathbf{s}_{f_i} of all fracture sets (e.g., Schoenberg and Muir, 1989; Hood, 1991):

$$\mathbf{s} = \mathbf{s}_b + \sum_{i=1}^N \mathbf{s}_{f_i}. \quad (\text{A2})$$

The compliances K_{ij} of each fracture set are mapped onto the corresponding compliance tensor s_{ijkl} using Hooke’s law (Schoenberg and Sayers, 1995):

$$s_{ijkl} = \frac{1}{4}(K_{ik}n_l n_j + K_{jk}n_i n_l + K_{il}n_j n_k + K_{jl}n_i n_k). \quad (\text{A3})$$

Equation (A1) indicates that \mathbf{K} is a 3×3 matrix that has to be symmetric and nonnegative definite because of the symmetries of the compliance tensor. Hence, a fracture system can be described by up to six independent compliance elements. The diagonal terms of the matrix relate the jumps in the normal displacement (“normal slips”) to the normal tractions acting across the surface of the fractures, as well as the tangential slips to the shear stresses. The off-diagonal elements are responsible for the coupling of the normal slips and shear stresses and vice-versa. Hereafter, we follow the notation of Grechka et al. (2003):

$$\begin{aligned} K_{11} &\rightarrow K_N; & K_{22} &\rightarrow K_V; & K_{33} &\rightarrow K_H; \\ K_{12} &\rightarrow K_{NV}; & K_{13} &\rightarrow K_{NH}; & K_{23} &\rightarrow K_{VH}. \end{aligned}$$

Here, we consider two vertical, orthogonal fracture sets oriented in such a way that the x_1 -axis is perpendicular to the first set. The summation in equation (A2) is more conveniently carried out using the condensed Voigt notation, which allows the compliance tensor to be replaced by a 6×6 compliance matrix. Then the compliances matrices for the two sets take the form

$$s_{f1} = \begin{pmatrix} K_{N1} & 0 & 0 & 0 & K_{NV1} & K_{NH1} \\ 0 & 0 & 0 & 0 & 0 & 0 \\ 0 & 0 & 0 & 0 & 0 & 0 \\ 0 & 0 & 0 & 0 & 0 & 0 \\ K_{NV1} & 0 & 0 & 0 & K_{V1} & K_{VH1} \\ K_{NH1} & 0 & 0 & 0 & K_{VH1} & K_{H1} \end{pmatrix}, \quad (\text{A4})$$

$$s_{f2} = \begin{pmatrix} 0 & 0 & 0 & 0 & 0 & 0 \\ 0 & K_{N2} & 0 & K_{NV2} & 0 & K_{NH2} \\ 0 & 0 & 0 & 0 & 0 & 0 \\ 0 & K_{NV2} & 0 & K_{V2} & 0 & K_{VH2} \\ 0 & 0 & 0 & 0 & 0 & 0 \\ 0 & K_{NH2} & 0 & K_{VH2} & 0 & K_{H2} \end{pmatrix}. \quad (\text{A5})$$

The compliance matrix of the isotropic background can be written as

$$s_b = \begin{pmatrix} E^{-1} & -\nu/E & -\nu/E & 0 & 0 & 0 \\ -\nu/E & E^{-1} & -\nu/E & 0 & 0 & 0 \\ -\nu/E & -\nu/E & E^{-1} & 0 & 0 & 0 \\ 0 & 0 & 0 & \mu^{-1} & 0 & 0 \\ 0 & 0 & 0 & 0 & \mu^{-1} & 0 \\ 0 & 0 & 0 & 0 & 0 & \mu^{-1} \end{pmatrix}, \quad (\text{A6})$$

where E is Young’s modulus and ν is Poisson’s ratio, which can be expressed through the Lamé parameters λ and μ :

$$E = \frac{\mu(3\lambda + 2\mu)}{\lambda + \mu}; \quad (\text{A7})$$

$$\nu = \frac{\lambda}{2(\lambda + \mu)}. \quad (\text{A8})$$

APPENDIX B: LINEARIZED STIFFNESS MATRIX FOR TWO ORTHOGONAL FRACTURE SETS

Wave phenomena are more conveniently described using the effective stiffness matrix that can be obtained by inverting the compliance matrix (A2). To simplify the resulting stiffness matrix, all stiffness elements can be linearized in the normalized quantities called fracture *weaknesses*. Following Grechka et al. (2003), the weaknesses for our model can be defined as

$$\Delta_{N_i} \equiv \frac{(\lambda + 2\mu) K_{N_i}}{1 + (\lambda + 2\mu) K_{N_i}}, \quad (\text{B1})$$

$$\Delta_{V_i} \equiv \frac{\mu K_{V_i}}{1 + \mu K_{V_i}}, \quad (\text{B2})$$

$$\Delta_{H_i} \equiv \frac{\mu K_{H_i}}{1 + \mu K_{H_i}}, \quad (\text{B3})$$

$$\Delta_{NV_i} \equiv \frac{\sqrt{\mu(\lambda + 2\mu)} K_{NV_i}}{1 + \sqrt{\mu(\lambda + 2\mu)} K_{NV_i}}, \quad (\text{B4})$$

$$\Delta_{NH_i} \equiv \frac{\sqrt{\mu(\lambda + 2\mu)} K_{NH_i}}{1 + \sqrt{\mu(\lambda + 2\mu)} K_{NH_i}}, \quad (\text{B5})$$

$$\Delta_{VH_i} \equiv \frac{\sqrt{\mu(\lambda + 2\mu)} K_{VH_i}}{1 + \sqrt{\mu(\lambda + 2\mu)} K_{VH_i}}, \quad (\text{B6})$$

where the subscript $i = 1, 2$ refers to the number of the fracture set. Since the matrix \mathbf{K} has to be nonnegative definite, the weaknesses satisfy the inequalities

$$\Delta_{IJ}^2 \leq \Delta_I \Delta_J, \quad (\text{B7})$$

where I and J denote the subscripts N , V , and H .

Using equations (A2) and (A4)–(A6) and linearizing the stiffness matrix $\mathbf{c} \equiv \mathbf{s}^{-1}$ in the fracture weaknesses [equations (B1)–(B6)], we obtain

$$\mathbf{c} \approx \begin{pmatrix} c_{11} & c_{12} & c_{13} & \chi c_{24} & c_{15} & c_{16} \\ c_{12} & c_{22} & c_{23} & c_{24} & \chi c_{15} & c_{26} \\ c_{13} & c_{23} & c_{33} & \chi c_{24} & \chi c_{15} & c_{36} \\ \chi c_{24} & c_{24} & \chi c_{24} & c_{44} & 0 & c_{46} \\ c_{15} & \chi c_{15} & \chi c_{15} & 0 & c_{55} & c_{56} \\ c_{16} & c_{26} & c_{36} & c_{46} & c_{56} & c_{66} \end{pmatrix}, \quad (\text{B8})$$

where

$$\chi \equiv \frac{\lambda}{\lambda + 2\mu}. \quad (\text{B9})$$

The linearized stiffness elements are given by

$$c_{11} \approx (\lambda + 2\mu) (1 - \Delta_{N_1} - \chi^2 \Delta_{N_2}), \quad (\text{B10})$$

$$c_{12} \approx \lambda (1 - \Delta_{N_1} - \Delta_{N_2}), \quad (\text{B11})$$

$$c_{13} \approx \lambda (1 - \Delta_{N_1} - \chi \Delta_{N_2}), \quad (\text{B12})$$

$$c_{14} \approx -\Delta_{NV_2} \sqrt{\lambda \mu \chi}, \quad (\text{B13})$$

$$c_{15} \approx -\Delta_{NV_1} \sqrt{\mu(\lambda + 2\mu)}, \quad (\text{B14})$$

$$c_{16} \approx -\sqrt{\mu(\lambda + 2\mu)} (\Delta_{NH_1} + \chi \Delta_{NH_2}), \quad (\text{B15})$$

$$c_{22} \approx (\lambda + 2\mu) (1 - \Delta_{N_2} - \chi^2 \Delta_{N_1}), \quad (\text{B16})$$

$$c_{23} \approx \lambda (1 - \chi \Delta_{N_1} - \Delta_{N_2}), \quad (\text{B17})$$

$$c_{24} \approx -\Delta_{NV_2} \sqrt{\mu(\lambda + 2\mu)}, \quad (\text{B18})$$

$$c_{25} \approx -\Delta_{NV_1} \sqrt{\lambda \mu \chi}, \quad (\text{B19})$$

$$c_{26} \approx -\sqrt{\mu(\lambda + 2\mu)} (\chi \Delta_{NH_1} + \Delta_{NH_2}), \quad (\text{B20})$$

$$c_{33} \approx (\lambda + 2\mu) [1 - \chi^2 (\Delta_{N_2} + \Delta_{N_1})], \quad (\text{B21})$$

$$c_{34} \approx -\Delta_{NV_2} \sqrt{\lambda \mu \chi}, \quad (\text{B22})$$

$$c_{35} \approx -\Delta_{NV_1} \sqrt{\lambda \mu \chi}, \quad (\text{B23})$$

$$c_{36} \approx -\sqrt{\lambda \mu \chi} (\Delta_{NH_1} + \Delta_{NH_2}), \quad (\text{B24})$$

$$c_{44} \approx \mu (1 - \Delta_{V_2}), \quad (\text{B25})$$

$$c_{45} \approx 0, \quad (\text{B26})$$

$$c_{46} \approx -\mu \Delta_{VH_2} \sqrt{\frac{\mu}{\lambda + 2\mu}}, \quad (\text{B27})$$

$$c_{55} \approx \mu (1 - \Delta_{V_1}), \quad (\text{B28})$$

$$c_{56} \approx -\mu \Delta_{VH_1} \sqrt{\frac{\mu}{\lambda + 2\mu}}, \quad (\text{B29})$$

$$c_{66} \approx \mu (1 - \Delta_{H_1} - \Delta_{H_2}). \quad (\text{B30})$$

If the weaknesses of the second fracture set are equal to zero, the linearized effective stiffnesses given above reduce to those obtained by Grechka et al. (2003) for a single microcorrugated fracture set orthogonal to the x_1 -axis. Another special case is that of rotationally invariant fractures, for which the off-diagonal weaknesses vanish and the tangential weaknesses Δ_{V_i} and Δ_{H_i} are equal to each other. If both fracture sets are made rotationally invariant, our stiffness matrix becomes identical to that in Bakulin et al. (2000b).